

A Novel Efficient Algorithm for Scattering from a Complex BOR Using Mixed Finite Elements and Cylindrical PML

Andrew D. Greenwood, *Member, IEEE*, and Jian-Ming Jin, *Senior Member, IEEE*

Abstract—An efficient finite-element method (FEM) is developed to compute scattering from a complex body of revolution (BOR). The BOR is composed of perfect conductor and impedance surfaces and arbitrary inhomogeneous materials. The method uses edge-based vector basis functions to expand the transverse field components and node-based scalar basis functions to expand the angular component. The use of vector basis functions eliminates the problem of spurious solutions suffered by other three component FEM formulations. The FEM mesh is truncated with a perfectly matched layer (PML) in cylindrical coordinates. The use of PML in cylindrical coordinates avoids the wasted computation which results from a spherical mesh boundary with an elongated scatterer. The FEM equations are solved by ordering the unknowns with a reverse Cuthill–McKee algorithm and applying a banded-matrix solution algorithm. The method is capable of handling large, realistic radar targets, and good agreement with measured results is achieved for benchmark targets.

Index Terms—Body of revolution, electromagnetic scattering, finite-element method, perfectly matched layer.

I. INTRODUCTION

A novel efficient algorithm to compute scattering from a complex body of revolution (BOR) is developed. The rotational symmetry of the scatterer allows the problem to be efficiently solved using a two-dimensional (2-D) computational method. Due to its importance as a radar target, the problem of scattering from a BOR has been studied extensively. The primary method is the method of moments (MoM) based on integral equation formulations [1]–[3]. This method works well for perfectly conducting or homogeneous bodies, but the computational complexity increases rapidly for inhomogeneous bodies. The computational complexity increases because a volume formulation, rather than a surface formulation, is required for an inhomogeneous target. The volume formulation, coupled with the fact that an integral equation generates a dense system of equations, greatly increases the computational complexity. Another popular method is the finite-difference method (FDM). This method results in a

sparse matrix and hence is computationally efficient. However, it relies on rectangular, cylindrical, or spherical computational grids, making it difficult to model arbitrarily shaped geometries [4]. The finite-element method (FEM) can effectively remove all of the above difficulties associated with the MoM and the FDM. For example, the FEM is much more versatile than the MoM because the same formulation is used for conducting, homogeneous, and inhomogeneous targets. Also, the FEM always generates a sparse system of equations, which is solved using much less computer memory and CPU time than a dense MoM matrix. Furthermore, the FEM conveniently and accurately models arbitrary shapes using triangular elements. As a result, the FEM has significant computational advantages for the problem of scattering from an arbitrary, inhomogeneous BOR.

Past FEM formulations for scattering from a BOR employ either the coupled azimuth potential (CAP) formulation [4]–[6] or the three-component node-based formulation [7]. In the CAP formulation, the problem is formulated in terms of the E_ϕ and H_ϕ field components. All other components are found in terms of E_ϕ , H_ϕ , and their derivatives. In the three-component node-based formulation, the problem is formulated in terms of E_ρ , E_ϕ , and E_z or in terms of H_ρ , H_ϕ , and H_z . Each component of \mathbf{E} or \mathbf{H} is expanded in terms of node-based, scalar basis functions. The three-component formulation has the advantage of yielding all three components of either the electric field or the magnetic field directly. However, using this formulation it is difficult to enforce the proper boundary conditions at material discontinuities and sharp conductor edges. This limits the kinds of material and scatterers that can be conveniently considered. Further, the three-component node-based formulation gives rise to nonphysical solutions known as spurious modes [7]. The problem of spurious modes can be overcome by the use of a penalty term, but it is difficult to choose the proper penalty factor.

The use of vector finite elements, also known as edge elements, eliminates many of the disadvantages of the three component, node-based formulation while retaining the advantage of computing either the electric field or the magnetic field directly. In the 2-D FEM, the transverse field components are expanded using a 2-D edge (vector) basis, and the longitudinal (ϕ) field component is expanded using a 2-D nodal (scalar) basis [8], [9]. At a material discontinuity, this expansion scheme automatically constrains the tangential field components to be continuous without similarly constraining the normal field

Manuscript received January 9, 1998; revised June 8, 1998. This work was supported by a grant from AFOSR via the MURI Program under contract F49620-96-1-0025, the Office of Naval Research under Grant N00014-95-1-0848, and the National Science Foundation under Grant NSF ECE 94-57735.

The authors are with the Center for Computational Electromagnetics, Department of Electrical and Computer Engineering, University of Illinois, Urbana, IL 61801 USA. D. Greenwood is also with Air Force Research Laboratory/DEPE, Kirtland AFB, NM 87117 USA.

Publisher Item Identifier S 0018-926X(99)04767-5.

It is more convenient to work with the scattered electric field than the total electric field. Thus, $\mathbf{E} = \mathbf{E}^i + \mathbf{E}^s$ is substituted into (6), and terms that do not depend on \mathbf{E}^s are dropped. This yields

$$\begin{aligned}
 F(\mathbf{E}^s) = & \frac{1}{2} \iiint_V \left[\frac{1}{\mu_r} (\nabla \times \mathbf{E}^s) \cdot \bar{\bar{\Lambda}}^{-1} \cdot (\nabla \times \mathbf{E}^s) \right. \\
 & \left. - k_0^2 \epsilon_r \mathbf{E}^s \cdot \bar{\bar{\Lambda}} \cdot \mathbf{E}^s \right] dV \\
 & + \frac{1}{2} \iint_{S_2} \gamma_e [\mathbf{E}^s \cdot \mathbf{E}^s - (\hat{n} \cdot \mathbf{E}^s)(\hat{n} \cdot \mathbf{E}^s)] dS \\
 & + \iint_{V^{sc}} \left[\frac{1}{\mu_r} (\nabla \times \mathbf{E}^s) \cdot \bar{\bar{\Lambda}}^{-1} \cdot (\nabla \times \mathbf{E}^i) \right. \\
 & \left. - k_0^2 \epsilon_r \mathbf{E}^s \cdot \bar{\bar{\Lambda}} \cdot \mathbf{E}^i \right] dV \\
 & + \iint_{S_2} \gamma_e [\mathbf{E}^s \cdot \mathbf{E}^i - (\hat{n} \cdot \mathbf{E}^s)(\hat{n} \cdot \mathbf{E}^i)] dS \\
 & - \iint_{S^{sc}} \mathbf{E}^s \cdot (\hat{n} \times \nabla \times \mathbf{E}^i) dS \quad (7)
 \end{aligned}$$

where V^{sc} is the region of a penetrable scatterer with $\mu_r \neq 1$ and/or $\epsilon_r \neq 1$, and S^{sc} is the boundary of this region, as shown in Fig. 1. Note that \hat{n} on S^{sc} points from the free space region into the penetrable scatterer region, and in the derivation of (7), the fact that $\nabla \times \nabla \times \mathbf{E}^i - k_0^2 \mathbf{E}^i = 0$ is used. To take advantage of the rotational symmetry of the problem, the fields are expanded in the Fourier modes as

$$\mathbf{E} = \sum_{m=-\infty}^{\infty} [\mathbf{E}_{t,m}(\rho, z) + \hat{\phi} E_{\phi,m}(\rho, z)] e^{jm\phi}. \quad (8)$$

The expansion in (8) is substituted into (7), and the integrations with respect to ϕ are then performed, yielding where Ω is the 2-D slice of V , C_2 is the 2-D slice of S_2 , and so forth, and

$$\bar{\bar{\Lambda}}_t = \hat{\rho} \hat{\rho} \Lambda_\rho + \hat{z} \hat{z} \Lambda_z; \quad \bar{\bar{\Lambda}}_t' = \hat{\rho} \hat{\rho} \Lambda_z + \hat{z} \hat{z} \Lambda_\rho. \quad (10)$$

The problem defined by (3)–(5) is now solved by seeking the stationary point of (9) subject to (4). To accomplish this task, an FEM expansion is substituted into (9), shown at the bottom of the page. An appropriate FEM expansion must consider the conditions that the field must satisfy at points along the z -axis. All field values must be continuous when the z -axis is approached along any $\phi = \text{constant}$ line. The conditions along the z -axis that ensure this are

$$E_{\rho,0} = E_{\phi,0} = (\nabla \times \mathbf{E})_{\rho,0} = (\nabla \times \mathbf{E})_{\phi,0} = 0 \quad (11)$$

for $m = 0$

$$\begin{aligned}
 E_{\rho,\pm 1} &= \mp j E_{\phi,\pm 1}, \quad (\nabla \times \mathbf{E})_{\rho,\pm 1} = \mp j (\nabla \times \mathbf{E})_{\phi,\pm 1}, \\
 E_{z,\pm 1} &= (\nabla \times \mathbf{E})_{z,\pm 1} = 0 \quad (12)
 \end{aligned}$$

for $m = \pm 1$ and

$$\begin{aligned}
 E_{\rho,m} &= E_{\phi,m} = E_{z,m} = (\nabla \times \mathbf{E})_{\rho,m} = (\nabla \times \mathbf{E})_{\phi,m} \\
 &= (\nabla \times \mathbf{E})_{z,m} = 0 \quad (13)
 \end{aligned}$$

for $|m| > 1$. FEM expansions which, together with a homogeneous Dirichlet condition on E_ϕ for $m \neq \pm 1$, satisfy these z -axis conditions are [14]

$$E_{\phi,0}^s = \sum_{i=1}^3 c_{\phi i}^e N_i^e, \quad \mathbf{E}_{t,0}^s = \sum_{i=1}^3 c_{ti}^e \mathbf{N}_i^e \quad (14)$$

for $m = 0$

$$\begin{aligned}
 E_{\phi,\pm 1}^s &= \sum_{i=1}^3 c_{\phi i}^e N_i^e \\
 \mathbf{E}_{t,\pm 1}^s &= \sum_{i=1}^3 [\mp j \hat{\rho} c_{\phi i}^e N_i^e + c_{ti}^e \rho \mathbf{N}_i^e] \quad (15)
 \end{aligned}$$

for $m = \pm 1$ and

$$E_{\phi,m}^s = \sum_{i=1}^3 c_{\phi i}^e N_i^e, \quad \mathbf{E}_{t,m}^s = \sum_{i=1}^3 c_{ti}^e \rho \mathbf{N}_i^e \quad (16)$$

$$\begin{aligned}
 F(\mathbf{E}^s) = & 2\pi \sum_{m=-\infty}^{\infty} \left\{ \frac{1}{2} \iint_{\Omega} \left\{ \frac{\rho}{\mu_r} \left[\frac{1}{\Lambda_\phi} (\nabla_t \times \mathbf{E}_{t,-m}^s) \cdot (\nabla_t \times \mathbf{E}_{t,m}^s) + \left(\nabla_t E_{\phi,-m}^s + \frac{jm}{\rho} \mathbf{E}_{t,-m}^s + \frac{\hat{\rho}}{\rho} E_{\phi,-m}^s \right) \cdot \bar{\bar{\Lambda}}_t'^{-1} \right. \right. \right. \\
 & \cdot \left(\nabla_t E_{\phi,m}^s - \frac{jm}{\rho} \mathbf{E}_{t,m}^s + \frac{\hat{\rho}}{\rho} E_{\phi,m}^s \right) \left. \right] - k_0^2 \epsilon_r \rho [\mathbf{E}_{t,-m}^s \cdot \bar{\bar{\Lambda}}_t \cdot \mathbf{E}_{t,m}^s + \Lambda_\phi E_{\phi,-m}^s E_{\phi,m}^s] \left. \right\} d\Omega \\
 & + \iint_{\Omega^{sc}} \left\{ \frac{\rho}{\mu_r} \left[(\nabla_t \times \mathbf{E}_{t,-m}^s) - \hat{\phi} \times \left(\nabla_t E_{\phi,-m}^s + \frac{jm}{\rho} \mathbf{E}_{t,-m}^s + \frac{\hat{\rho}}{\rho} E_{\phi,-m}^s \right) \right] \cdot \bar{\bar{\Lambda}}^{-1} \cdot (\nabla \times \mathbf{E}_m^i) \right. \\
 & \left. - k_0^2 \epsilon_r \rho [\mathbf{E}_{t,-m}^s \cdot \bar{\bar{\Lambda}}_t \cdot \mathbf{E}_{t,m}^i + \Lambda_\phi E_{\phi,-m}^s E_{\phi,m}^i] \right\} d\Omega + \frac{1}{2} \int_{C_2} \gamma_e \rho [\mathbf{E}_{t,-m}^s \cdot \mathbf{E}_{t,m}^s \\
 & - (\hat{n} \cdot \mathbf{E}_{t,-m}^s)(\hat{n} \cdot \mathbf{E}_{t,m}^s) + E_{\phi,-m}^s E_{\phi,m}^s] d\ell + \int_{C_2} \gamma_e \rho [\mathbf{E}_{t,-m}^s \cdot \mathbf{E}_{t,m}^i - (\hat{n} \cdot \mathbf{E}_{t,-m}^s)(\hat{n} \cdot \mathbf{E}_{t,m}^i) \\
 & + E_{\phi,-m}^s E_{\phi,m}^i] d\ell - \int_{C^{sc}} \rho [\mathbf{E}_{t,-m}^s + \hat{\phi} E_{\phi,-m}^s] \cdot [\hat{n} \times (\nabla \times \mathbf{E}_m^i)] d\ell \left. \right\} \quad (9)
 \end{aligned}$$

for $|m| > 1$, where N_i^e is a standard 2-D nodal-element basis function, and \mathbf{N}_i^e is a standard 2-D edge-element basis function. When the FEM expansions are substituted into (9), a system of the form

$$F(\mathbf{E}^s) = \sum_{m=-\infty}^{\infty} \left(\frac{1}{2} \left\{ \begin{matrix} e_t^{-m} \\ e_\phi^{-m} \end{matrix} \right\}^T \begin{bmatrix} A_{tt}^m & A_{t\phi}^m \\ A_{\phi t}^m & A_{\phi\phi}^m \end{bmatrix} \left\{ \begin{matrix} e_t^m \\ e_\phi^m \end{matrix} \right\} - \left\{ \begin{matrix} e_t^{-m} \\ e_\phi^{-m} \end{matrix} \right\}^T \left\{ \begin{matrix} B_t^m \\ B_\phi^m \end{matrix} \right\} \right) \quad (17)$$

results where $[A_{tt}^m]$, $[A_{t\phi}^m]$, $[A_{\phi t}^m]$, $[A_{\phi\phi}^m]$, $\{B_t^m\}$, and $\{B_\phi^m\}$ are all assembled from the elemental matrices and vectors which are obtained directly from the substitution of (14)–(16) into (9). Note that $[A_{tt}^m]$ and $[A_{\phi\phi}^m]$ are symmetric and $[A_{t\phi}^m] = [A_{\phi t}^m]^T$ so that the entire matrix in (17) is symmetric in addition to being sparse. The stationary point of the functional is found by differentiating (17) with respect to

$$\left\{ \begin{matrix} e_t^{-m} \\ e_\phi^{-m} \end{matrix} \right\}^T$$

and setting the result to zero, giving systems of the form

$$\begin{bmatrix} A_{tt}^m & A_{t\phi}^m \\ A_{\phi t}^m & A_{\phi\phi}^m \end{bmatrix} \left\{ \begin{matrix} e_t^m \\ e_\phi^m \end{matrix} \right\} = \left\{ \begin{matrix} B_t^m \\ B_\phi^m \end{matrix} \right\}; \quad m = 0, \pm 1, \pm 2, \dots \quad (18)$$

It can be shown that

$$\begin{aligned} \{e_t^m\} &= \begin{cases} \{e_t^{-m}\} & \text{V-pol incidence} \\ -\{e_t^{-m}\} & \text{H-pol incidence} \end{cases} \\ \{e_\phi^m\} &= \begin{cases} -\{e_\phi^{-m}\} & \text{V-pol incidence} \\ \{e_\phi^{-m}\} & \text{H-pol incidence} \end{cases} \end{aligned} \quad (19)$$

for all $m \neq 0$. Thus, the solution of the FEM equations is needed for positive numbered modes only.

B. PML

To limit the number of unknowns in the FEM equations, the mesh must be truncated. PML absorbers are used to attenuate reflections from the artificial outer boundary, where the condition $\hat{n} \times \mathbf{E}^s = 0$ is applied. The diagonal tensor $\bar{\bar{\Lambda}}$ in (1) contains the properties of the PML. In order to effectively eliminate artificial reflections, the PML to air interface must be reflectionless in cylindrical coordinates, and waves which propagate through the PML must be attenuated. These conditions are satisfied when the elements of $\bar{\bar{\Lambda}}$ are given by [11] and [12]

$$\Lambda_\rho = \frac{S_z \tilde{\rho}}{S_\rho \rho}; \quad \Lambda_\phi = \frac{S_z S_\rho \rho}{\tilde{\rho}}; \quad \Lambda_z = \frac{S_\rho \tilde{\rho}}{S_z \rho} \quad (20)$$

TABLE I
RELATIVE ERROR IN DECIBELS AS A FUNCTION OF α

α	$m = 0$	$m = 1$	$m = 2$	$m = 3$
2.0	-19.01	-16.23	-17.92	-20.53
5.0	-44.79	-42.67	-34.73	-44.21
10.0	-44.19	-40.79	-35.48	-44.42
15.0	-41.67	-37.22	-35.50	-44.40
20.0	-39.40	-34.80	-35.31	-40.58
25.0	-38.89	-34.18	-35.86	-39.86

in which

$$S_\rho = S_\rho(\rho) = \begin{cases} 1 & 0 \leq \rho \leq \rho_m \\ 1 - j\alpha \left(\frac{\rho - \rho_m}{t_\rho} \right)^2 & \rho > \rho_m \end{cases} \quad (21)$$

$$S_z = S_z(z) = \begin{cases} 1 - j\alpha \left(\frac{z_{ml} - z}{t_{zl}} \right)^2 & z < z_{ml} \\ 1 & z_{ml} \leq z \leq z_{mu} \\ 1 - j\alpha \left(\frac{z - z_{mu}}{t_{zu}} \right)^2 & z > z_{mu} \end{cases} \quad (22)$$

$$\tilde{\rho} = \begin{cases} \rho & 0 \leq \rho \leq \rho_m \\ \rho - j\alpha \frac{(\rho - \rho_m)^3}{3t_\rho^2} & \rho > \rho_m \end{cases} \quad (23)$$

where t_ρ , t_{zl} , and t_{zu} are the PML thicknesses; $\rho = \rho_m$, $z = z_{ml}$, and $z = z_{mu}$ are the locations of the air to PML interfaces (see Fig. 1); and α is a real parameter to be selected. While the PML to air interface is reflectionless in continuous space, some spurious reflection results from the discretization of the FEM mesh. Smaller values of α lower the contrast at the air to PML interface, thus reducing this spurious reflection, while larger values of α increase the attenuation of waves propagating through the PML. Thus, there is a tradeoff in the selection of the PML loss parameter α .

The tradeoff in the selection of α is investigated by exciting a current loop in a free-space FEM mesh and examining the relative error in the fields computed by the FEM code. The results of such an investigation are presented in Table I. The values in Table I are computed with a mesh length of $\lambda/20$ and a PML thickness of 0.25λ . The relative error values in the table exhibit little change over a large range of α values, indicating that the discretization error in the mesh rather than spurious reflection from the boundary is dominating the error values. The PML parameter α is further investigated by computing the far field bistatic RCS of a conducting sphere of radius 2λ and comparing to the exact Mie series result. In Fig. 2, the absolute value of the error between the FEM computation and the Mie result is averaged over 181 observation angles and plotted as a function of α . Both the values in Table I and the plots in Fig. 2 show that for a mesh length of $\lambda/20$ and a PML thickness of 0.25λ , the optimum value of α is around 5.5–6.0.

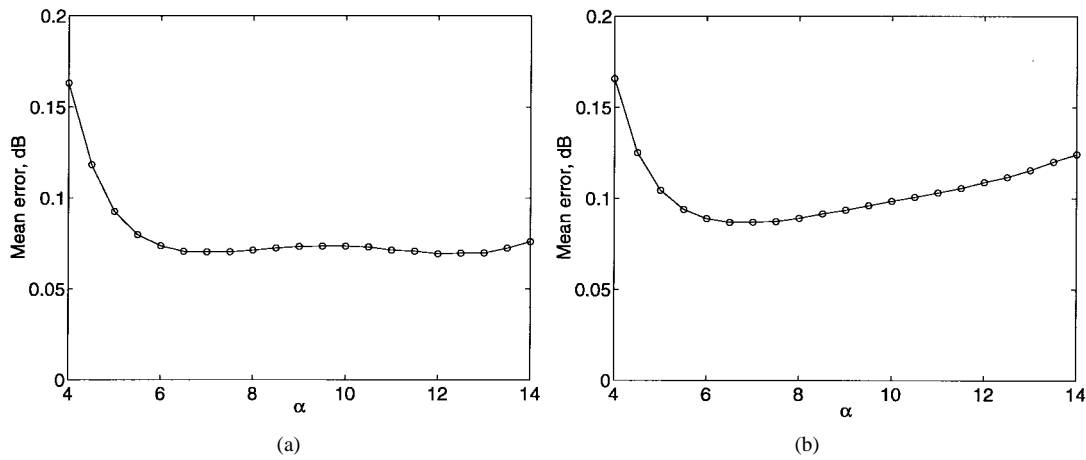


Fig. 2. Mean error in the bistatic RCS of a conducting sphere ($r = 2\lambda$) as a function of the PML parameter α . (a) VV-polarization. (b) HH-polarization.

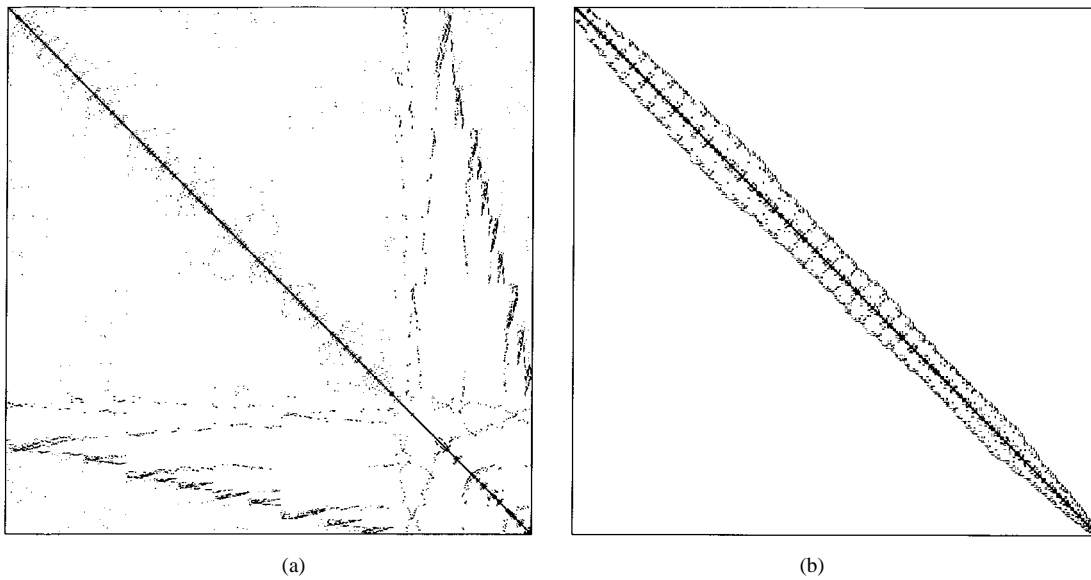


Fig. 3. Sparsity pattern of an FEM matrix with 5000 unknowns. (a) Original ordering. (b) RCM ordering.

C. Solution of the Equations

The solution of a scattering problem by the FEM involves the assembly and solution of the system of equations of the form of (18). As mentioned in Section II-A, the matrix of (18) is sparse and symmetric. Also, in (18), the excitation vector $\{B\}$ is a function of the incidence angle and the polarization of the incident field, but the FEM matrix $[A]$ is not. Thus, if the solution is computed by matrix decomposition techniques, the decomposition of the matrix is computed only once, even if the solution corresponding to multiple incidence angles and polarizations is required. Finally, when the unknowns are ordered according to the reverse Cuthill–McKee (RCM) ordering, the FEM matrix is highly banded. The RCM algorithm is discussed in [15] and a typical result for a case with 5000 unknowns is shown in Fig. 3.

The steps in solving the FEM equations are first, using the RCM ordering, the FEM matrix for a given mode number (m) is assembled. In each row of the matrix, the first nonzero element through the diagonal element are stored in an array.

This storage scheme facilitates the second step of the solution, the efficient decomposition of the matrix by a band solver. The band solver employed computes the LDL^T decomposition of the matrix using Crout decomposition techniques in $O(NB^2)$ computational complexity where N is the number of unknowns and B is the matrix half-bandwidth [13]. After factoring the matrix, the third solution step is to assemble an excitation vector; then, the fourth step is the solution of triangular systems using forward and back substitutions in $O(NB)$ computational complexity. The contribution of mode m to the radar cross section (RCS) of the target is then computed and the next step is to repeat the assembly of an excitation vector, the forward and back substitutions, and the RCS calculation for each incidence angle and polarization. The final step is the repetition of the whole process for each mode number required. A rule of thumb for the number of modes required is $M_{\max} = k_0 \rho_{\max} \sin \theta + 6$ [1]. This rule of thumb is valid for $k_0 \rho_{\max} \sin \theta > 3$.

It is of note that a minimum degree ordering of the unknowns, which seeks to minimize the number of nonzeros

on the factored matrix, may offer improved efficiency in the matrix solution. For example, some preliminary experiments show that the matrix storage can be reduced to about half of the current banded storage.

D. RCS Calculation

The solution of the FEM equations yields the scattered electric field near the scatterer. Because the far-field RCS of the target is often of interest, the scattered electric field far from the scatterer is computed from near-field values. Consider an infinitesimal dipole, located at the scattering observation point, oriented in the \hat{u} direction, and excited such that it produces a plane wave of unit amplitude at the coordinate origin. Denoting the far-field scattered electric field of the target as $\mathbf{E}^s(R)$ and the field radiated by the dipole as \mathbf{E}^r , by reciprocity

$$\mathbf{E}^s(R) \cdot \hat{u} = \frac{e^{-jk_0 R}}{4\pi R} \iint_{S'} [\mathbf{E}^r \cdot (\hat{n} \times \nabla \times \mathbf{E}^s) + (\nabla \times \mathbf{E}^r) \cdot (\hat{n} \times \mathbf{E}^s)] dS' \quad (24)$$

where S' is any rotationally symmetric, closed surface which encloses the entire scatterer. The fields in (24) are expanded according to (8), and the ϕ integration is performed, giving

$$\mathbf{E}^s(R) \cdot \hat{u} = \frac{e^{-jk_0 R}}{2R} \sum_{m=-\infty}^{\infty} j^m e^{jm\phi^r} \cdot \int_{C'} \rho' [\mathbf{E}_{-m}^r \cdot (\hat{n} \times \nabla \times \mathbf{E}_m^s) + (\nabla \times \mathbf{E}_{-m}^r) \cdot (\hat{n} \times \mathbf{E}_m^s)] d\ell' \quad (25)$$

where θ^r and ϕ^r denote the scattering observation direction. The components of $\mathbf{E}^s(R)$ which are of interest, are the vertically polarized component $E_\theta^s(R)$ and the horizontally polarized component $E_\phi^s(R)$. For $\hat{u} = \hat{\theta}$ and $\hat{u} = \hat{\phi}$, expressions for \mathbf{E}_{-m}^r and $(\nabla \times \mathbf{E}_{-m}^r)$ are found by expanding the dipole radiated fields according to (8) and these expressions are substituted into (25), giving

$$\begin{aligned} E_\theta^s(R) = & \frac{e^{-jk_0 R}}{2R} \sum_{m=-\infty}^{\infty} j^m e^{jm\phi^r} \int_{C'} \rho' e^{jk_0 z' \cos \theta^r} \\ & \cdot \left\{ (\hat{n} \times \nabla \times \mathbf{E}_m^s) \cdot \left[-\hat{\rho} \cos \theta^r j J'_m(k_0 \rho' \sin \theta^r) \right. \right. \\ & - \hat{\phi} \cos \theta^r \frac{m J_m(k_0 \rho' \sin \theta^r)}{k_0 \rho' \sin \theta^r} \\ & \left. \left. - \hat{z} \sin \theta^r J_m(k_0 \rho' \sin \theta^r) \right] + k_0 (\hat{n} \times \mathbf{E}_m^s) \right. \\ & \left. \cdot \left[\hat{\rho} j \frac{m J_m(k_0 \rho' \sin \theta^r)}{k_0 \rho' \sin \theta^r} + \hat{\phi} J'_m(k_0 \rho' \sin \theta^r) \right] \right\} d\ell' \quad (26) \end{aligned}$$

$$\begin{aligned} E_\phi^s(R) = & \frac{e^{-jk_0 R}}{2R} \sum_{m=-\infty}^{\infty} j^m e^{jm\phi^r} \int_{C'} \rho' e^{jk_0 z' \cos \theta^r} \\ & \cdot \left\{ (\hat{n} \times \nabla \times \mathbf{E}_m^s) \right. \\ & \cdot \left[\hat{\rho} \frac{m J_m(k_0 \rho' \sin \theta^r)}{k_0 \rho' \sin \theta^r} - \hat{\phi} j J'_m(k_0 \rho' \sin \theta^r) \right] \\ & + k_0 (\hat{n} \times \mathbf{E}_m^s) \\ & \cdot \left[-\hat{\rho} \cos \theta^r J'_m(k_0 \rho' \sin \theta^r) \right. \\ & + \hat{\phi} \cos \theta^r j \frac{m J_m(k_0 \rho' \sin \theta^r)}{k_0 \rho' \sin \theta^r} \\ & \left. \left. + \hat{z} \sin \theta^r j J_m(k_0 \rho' \sin \theta^r) \right] \right\} d\ell' \quad (27) \end{aligned}$$

and where $J_m(x)$ denotes the Bessel function of order m and $J'_m(x)$ denotes the derivative of $J_m(x)$ with respect to its argument. The RCS of the scatterer is found from the definition

$$\sigma = \lim_{R \rightarrow \infty} 4\pi R^2 \frac{|\mathbf{E}^s(R)|^2}{|\mathbf{E}^i(R)|^2}. \quad (28)$$

III. NUMERICAL EXAMPLES

A number of numerical results are presented to show the validity and capability of the FEM technique. Unless otherwise stated, mesh length for each example is $\lambda/20$, and the air to PML interface is placed 0.25λ from the target.

First, in Fig. 4 the bistatic RCS of a coated sphere is computed and compared to the exact Mie series solution. The incident elevation angle is 90° , and the conducting core of the sphere has a radius of 2λ . The target is coated with ferrite 0.1λ thick, and the ferrite coating is characterized by $\epsilon_r = 2.5 - j1.25$ and $\mu_r = 1.6 - j0.8$. The mesh is truncated with a PML 0.25λ thick with $\alpha = 5.0$. The comparison in Fig. 4 shows a maximum error of 0.57 dB in the VV-polarized case and 0.74 dB in the HH-polarized case, which is good agreement considering the dynamic range of over 40 dB in the RCS.

Next, a number of electromagnetic code consortium (EMCC) benchmark targets are considered, and the FEM results are compared to measurements first published in [16], where detailed descriptions of the targets are also found. To establish a reference on the capability of the code, information about the memory and CPU time required to generate the monostatic scattering results for two polarizations and 181 incidence angles on a 44 Mflop DEC Alpha workstation is also presented in Table II. For the EMCC benchmark targets, the mesh is truncated with a PML 0.5λ thick with $\alpha = 10$.

The first EMCC benchmark target is a metallic ogive, shown in Fig. 5. The ogive has a length of 10 in, a maximum diameter of 2 in, and a half-angle of 22.62° at each tip. Both the monostatic VV-polarized and the monostatic HH-polarized RCS of the ogive at 9 GHz are computed and compared to measurements in Fig. 5. The agreement in Fig. 5 is generally good, however, some error is observed around 15° elevation

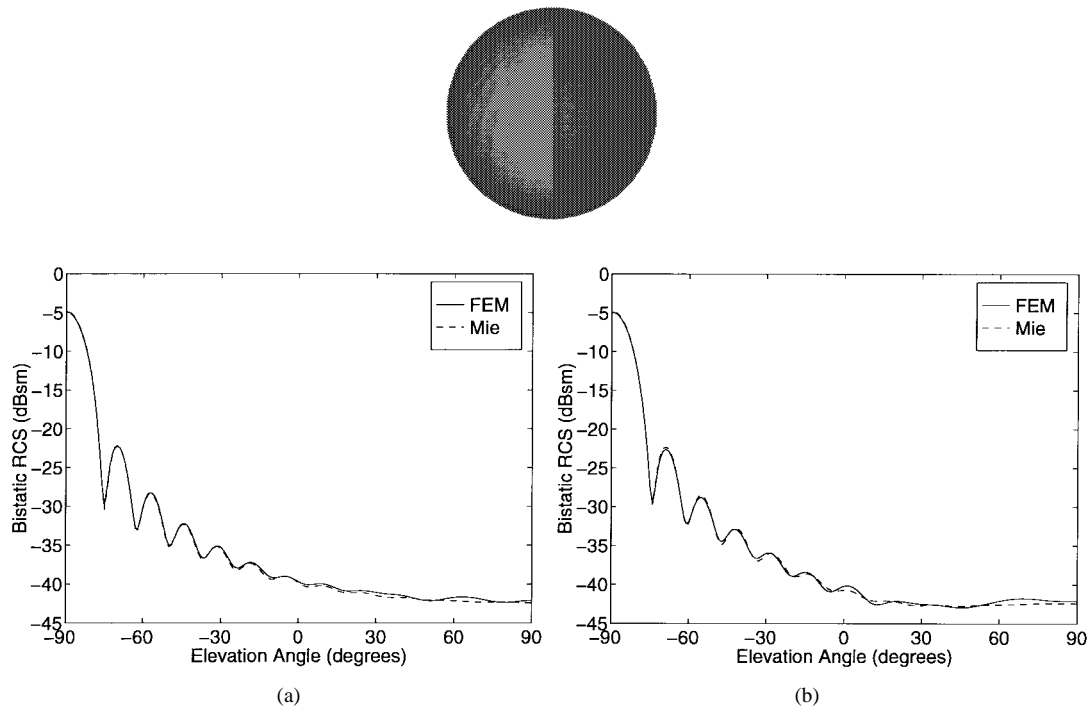


Fig. 4. RCS of a coated sphere with an incident elevation angle of 90° . The radius of the conducting core is 2λ , and the coating is 0.1λ thick with $\epsilon_r = 2.5 - j1.25$ and $\mu_r = 1.6 - j0.8$. (a) VV-polarization. (b) HH-polarization.

TABLE II
MEMORY AND CPU REQUIREMENTS TO COMPUTE MONOSTATIC
SCATTERING FOR TWO POLARIZATIONS AND 181 INCIDENCE
ANGLES ON A 44 MFLOP DEC ALPHA WORKSTATION

Target	Number of Unknowns	Matrix Half- Bandwidth	Memory (Mbytes)	CPU Time (min.)
Ogive	18,429	197	13	25.5
Double Ogive	15,348	201	11	21.3
Conesphere	42,960	386	33	137.1
Conesphere with gap	42,848	379	33	135.1
Coated Conesphere	47,743	368	39	182.9
Missile	70,604	319	40	233.6

for both polarizations. This error must be caused by errors in measurement as the target is symmetric about the 0° elevation plane. There is also some error observed near the bottom of the dynamic range in the HH-polarized case. This error is also caused by measurement errors.

The second EMCC benchmark target is a metallic double ogive, shown in Fig. 6. The double ogive is formed by joining two different half-ogives. The top piece has a half-length of 5 in, a maximum radius of 1 in, and a half-angle of 22.62° at the tip, and the bottom has a half-length of 2.5 in, a maximum radius of 1 in, and a half-angle of 46.4° at the tip. The computed monostatic RCS of the double ogive at 9 GHz is compared to measurements in Fig. 6, and except for some discrepancy near the bottom of the dynamic range, the agreement is generally good. Similar to the ogive example, the error is caused by measurement error.

A third EMCC benchmark is a metallic conesphere, shown in Fig. 7. The sphere has a radius of 2.947 in, the cone tip has a half-angle of 7° , the cone is 23.821 in tall, and the cone

is tangent to the sphere at the junction. The monostatic RCS at 9 GHz is computed and a comparison to measured values is shown in Fig. 7. In computing the result for this target, portions of the mesh between the conesphere and the PML interface are coarsened to a mesh length of $\lambda/10$. This reduces the number of unknowns in the problem, which becomes large because the target is over 20λ long. A good agreement is observed in Fig. 7.

The final EMCC benchmark target is similar to the metallic conesphere considered in the previous example. The only difference is a 0.25 in wide \times 0.25 in deep gap located at the junction between the cone and the sphere. The comparison of measured results to computed results at 9 GHz in Fig. 8 shows good agreement, and comparing Figs. 7 and 8 shows that the gap has a large influence on the RCS of the target at this frequency. Similar to the previous example, the mesh for the computed results in this example is coarsened to $\lambda/10$ mesh length in regions between the target and the PML.

To further show the utility of the method, two more computed results are presented. The first of these is the EMCC benchmark conesphere, again at 9 GHz, but coated with 0.131 in (0.1λ) thick ferrite ($\epsilon_r = 2.5 - j1.25$, $\mu_r = 1.6 - j0.8$). The RCS is shown in Fig. 9, and comparison between Figs. 7 and 9 show that the coating has lowered the RCS 10–15 dB. The primary increase in CPU time from the metallic conesphere case to this coated example (see Table II) is due to the slight increase in ρ_{\max} for the target, which causes the rule of thumb of Part C of Section II to predict an increase in the number of modes required. However, the expected CPU time increase from an integral equation method applied to the same two problems is much greater than the factor of 1.25 observed here. The second example is a SCUD-like missile, shown in

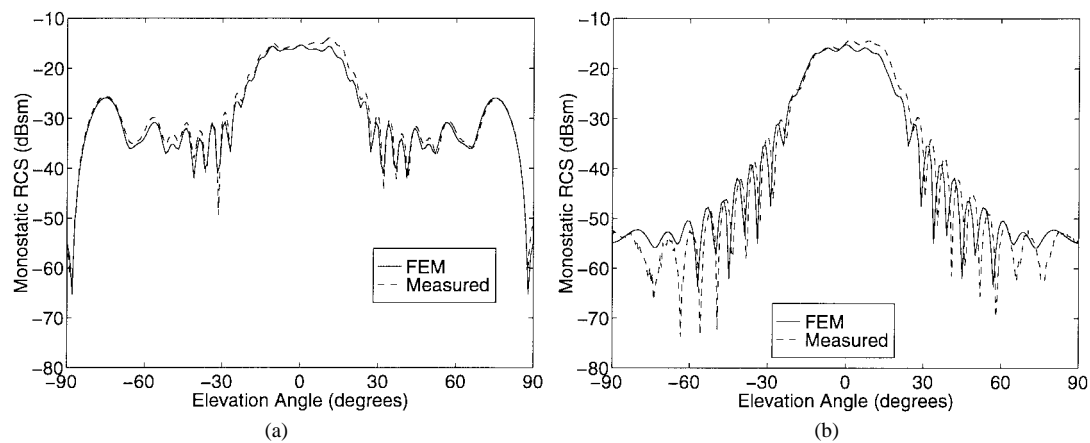


Fig. 5. RCS of a metallic ogive at 9 GHz. The ogive has a height of 10 in (7.63λ), a maximum diameter of 2 in (1.53λ), and a half-angle of 22.62° at the tip. (a) VV-polarization. (b) HH-polarization.

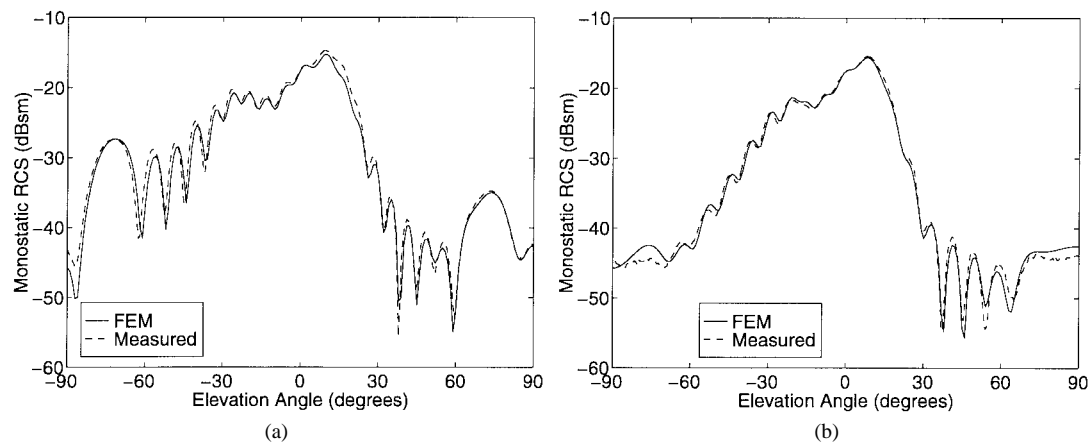


Fig. 6. RCS of a metallic double ogive at 9 GHz. The top piece of the double ogive has a half-height of 5 in (3.81λ), a maximum radius of 1 in (0.763λ), and a half-angle of 22.62° at the tip, and the bottom has a half-height of 2.5 in (1.91λ), a maximum radius of one in (0.763λ), and a half-angle of 46.4° at the tip. (a) VV-polarization. (b) HH-polarization.

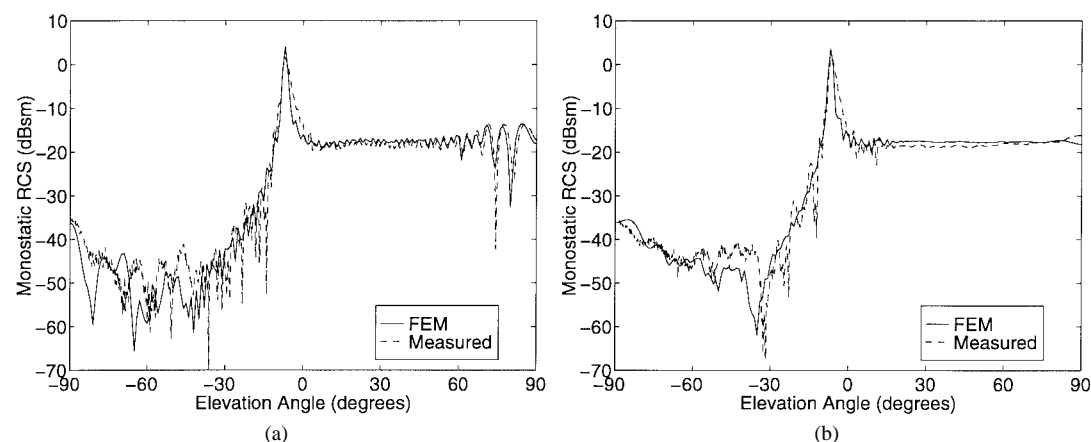


Fig. 7. RCS of a metallic conesphere at 9 GHz. The sphere has a radius of 2.947 in (2.247λ); the cone has a half-angle of 7° at the tip and a length of 23.821 in (18.164λ), and the cone is tangent to the sphere at the junction point. (a) VV-polarization. (b) HH-polarization.

Fig. 10. The missile has a metallic core coated with 3 cm (0.1λ at 1 GHz) thick ferrite ($\epsilon_r = 2.5 - j1.25$, $\mu_r = 1.6 - j0.8$). The missile is 12.5 m tall, and, as shown in Fig. 10, there are several 3 cm wide by 3 cm deep ($0.1\lambda \times 0.1\lambda$ at 1 GHz) gaps on its surface. Its RCS at 1 GHz is shown in Fig. 10.

Finally, to show the application of the method to dielectric scatterers, a spherical Luneburg lens is considered. The Luneburg lens is characterized by a relative permittivity of $\epsilon_r = 2 - (r/a)^2$ where r is the distance from the center of the lens and a is the radius of the lens [17]. The scattering from a

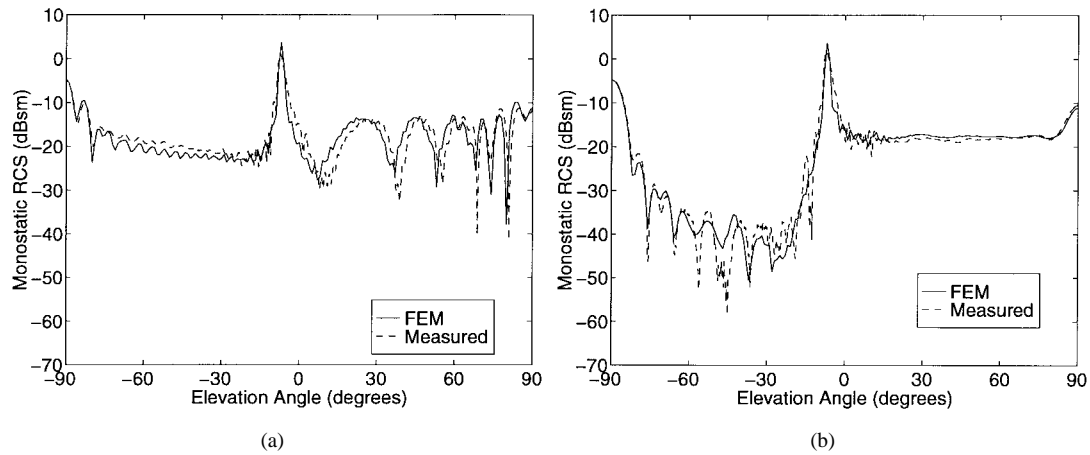


Fig. 8. RCS of a metallic conesphere with a gap at 9 GHz. The sphere has a radius of 2.947 in (2.247λ), and the cone has a half-angle of 7° at the tip and a length of 23.821 in (18.164λ). At the junction between the cone and the sphere, there is a 0.25-in-wide by 0.25-in-deep ($0.19\lambda \times 0.19\lambda$) gap. (a) VV-polarization. (b) HH-polarization.

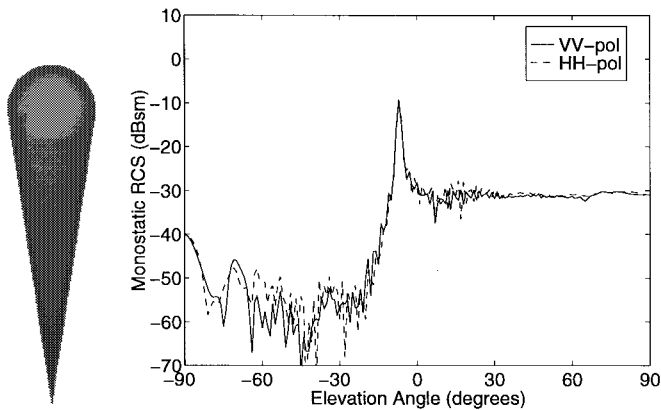


Fig. 9. RCS of a coated metallic conesphere at 9 GHz. The conesphere is coated with 0.13 in (0.1λ) thick ferrite ($\epsilon_r = 2.5 - j1.25$, $\mu_r = 1.6 - j0.8$). The sphere has a radius of 2.947 in (2.247λ); the cone has a half-angle of 7° at the tip and a length of 23.821 in (18.164λ), and the cone is tangent to the sphere at the junction point.

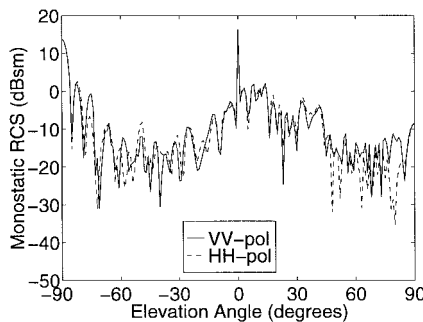
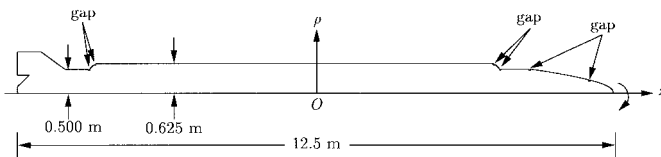


Fig. 10. RCS of a SCUD-like missile at 1 GHz. The missile is a conducting core coated with 3 cm (0.1λ) thick ferrite ($\epsilon_r = 2.5 - j1.25$, $\mu_r = 1.6 - j0.8$), and it is 12.5 meters (41.7λ) tall. As shown, there are several 3 cm wide by 3 cm deep ($0.1\lambda \times 0.1\lambda$) gaps on the missile surface.

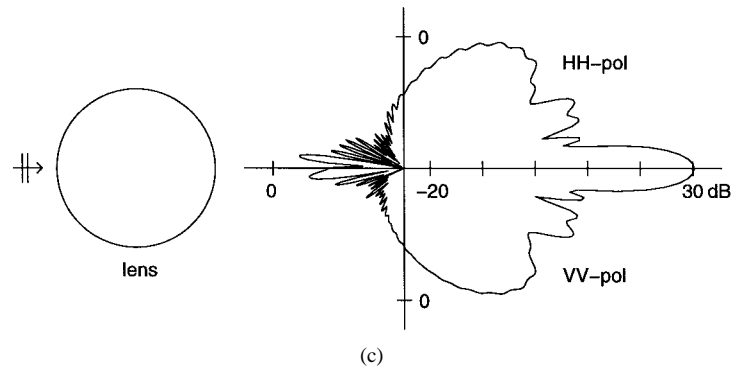
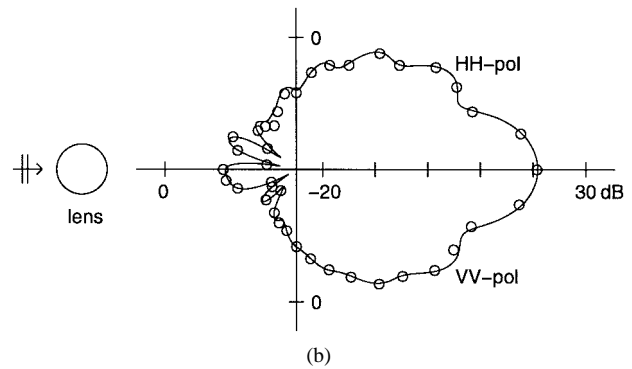
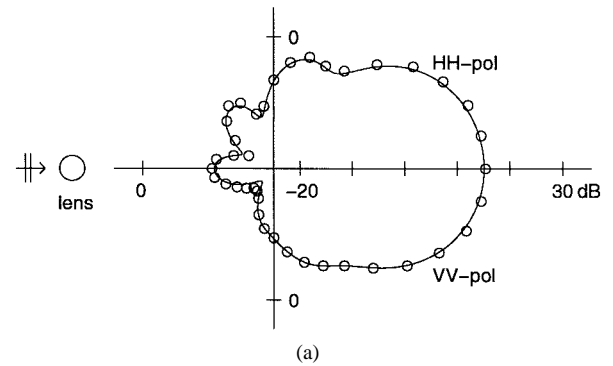


Fig. 11. Bistatic RCS of a spherical Luneburg lens. The lens has permittivity $\epsilon_r = 2 - (r/a)^2$, and the circles represent data given in [17]. (a) $k_o a = 5$. (b) $k_o a = 10$. (c) $k_o a = 31.4$.

Luneburg lens of three different sizes is shown in Fig. 11. For the first two lenses, note the agreement with data given in [17].

The numerical results presented show the validity and utility of the method. Good agreement is achieved in the comparison with exact techniques and with measurements. Further, it is seen that large radar targets with inhomogeneous materials can be considered.

IV. CONCLUSION

A novel efficient FEM algorithm to compute the scattering from an arbitrary BOR is developed. Because of its versatility in modeling complex shapes and inhomogeneous materials, the FEM possesses advantages over other computational methods in its ability to handle arbitrary BOR's. For instance, by using triangular elements, the FEM can more accurately model arbitrarily shaped geometries than can FDM's, which rely on rectangular, cylindrical, or spherical grids. Also, the FEM can handle inhomogeneous materials without the large increase in computational complexity found in integral equation methods. By using mixed finite elements, the FEM can compute either the electric field or the magnetic field directly, without the problems posed to other three-component formulations by material discontinuities and spurious solutions. Cylindrical PML efficiently and accurately truncates the FEM mesh, without requiring a spherical boundary, a large distance between the scatterer and the boundary, or an increase in the matrix bandwidth. The FEM algorithm using mixed finite elements and PML shows good agreement with exact techniques and with measured data, and it effectively handles both penetrable and impenetrable targets as well as large targets with inhomogeneous materials.

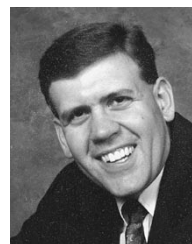
ACKNOWLEDGMENT

The authors would like to thank W. D. Wood for providing the EMCC measured data.

REFERENCES

- [1] M. G. Andreasen, "Scattering from bodies of revolution," *IEEE Trans. Antennas Propagat.*, vol. AP-13, pp. 303–310, Mar. 1965.
- [2] J. R. Mautz and R. F. Harrington, "Electromagnetic scattering from a homogeneous body of revolution," *Arch. Elektron. Ubertragungstech.*, vol. 33, pp. 71–80, 1979.
- [3] L. N. Medgyesi-Mitschang and J. M. Putnam, "Electromagnetic scattering from axially inhomogeneous bodies of revolution," *IEEE Trans. Antennas Propagat.*, vol. AP-32, pp. 797–806, Aug. 1984.
- [4] R. Gordon and R. Mittra, "PDE techniques for solving the problem of radar scattering by a body of revolution," *Electromagn.*, vol. 10, pp. 163–174, 1990.
- [5] M. A. Morgan, S. K. Chang, and K. K. Mei, "Coupled azimuth potentials for electromagnetic field problems in inhomogeneous axially symmetric media," *IEEE Trans. Antennas Propagat.*, vol. AP-25, pp. 413–417, May 1977.
- [6] M. A. Morgan and K. K. Mei, "Finite-element computation of scattering by inhomogeneous penetrable bodies of revolution," *IEEE Trans. Antennas Propagat.*, vol. AP-27, pp. 202–214, Mar. 1979.
- [7] A. Khebir, J. D'Angelo, and J. Joseph, "A new finite element formulation for RF scattering by complex bodies of revolution," *IEEE Trans. Antennas Propagat.*, vol. 41, pp. 534–541, May 1993.
- [8] J. F. Lee, G. Wilkins, and R. Mittra, "Finite-element analysis of an axisymmetric cavity resonator using a hybrid edge element technique," *IEEE Trans. Microwave Theory Tech.*, vol. 41, pp. 1981–1987, Nov. 1993.

- [9] D. J. Hoppe, L. Epp, and J. F. Lee, "A hybrid symmetric FEM/MOM formulation applied to scattering by inhomogeneous bodies of revolution," *IEEE Trans. Antennas Propagat.*, vol. 42, pp. 798–805, June 1994.
- [10] W. C. Chew, J. M. Jin, and E. Michielssen, "Complex coordinate stretching as a generalized absorbing boundary condition," in *13th Annu. Rev. Progress Appl. Comput. Electromagn.*, Monterey, CA, vol. II, pp. 909–914, Mar. 1997.
- [11] F. L. Teixeira and W. C. Chew, "Systematic derivation of anisotropic PML absorbing media in cylindrical and spherical coordinates," *IEEE Microwave Guided Wave Lett.*, vol. 7, pp. 371–373, Nov. 1997.
- [12] J. Maloney, M. Kesler, and G. Smith, "Generalization of {PML} to cylindrical geometries," in *13th Annu. Rev. Progress Appl. Comput. Electromagn.*, Monterey, CA, vol. II, pp. 900–908, Mar. 1997.
- [13] J. M. Jin, *The Finite Element Method in Electromagnetics*. New York: Wiley, 1993.
- [14] M. F. Wong, M. Prak, and V. F. Hanna, "Axisymmetric edge-based finite element formulation for bodies of revolution: Application to dielectric resonators," in *IEEE MTT-S Dig.*, pp. 285–288, May 1995.
- [15] A. George and J. W. Liu, *Computer Solution of Large Sparse Positive Definite Systems*. Englewood Cliffs, NJ: Prentice-Hall, 1981.
- [16] A. C. Woo, H. T. G. Wang, M. J. Schuh, and M. L. Sanders, "Benchmark radar targets for the validation of computational electromagnetics programs," *IEEE Antennas Propagat. Mag.*, vol. 35, pp. 84–89, Feb. 1993.
- [17] P. Rozenfeld, "The electromagnetic theory of three-dimensional inhomogeneous lenses," *IEEE Trans. Antennas Propagat.*, vol. 24, pp. 365–370, May 1976.



Andrew D. Greenwood (S'90–M'98) was born November 11, 1968 in Ogden, UT. He received the Bachelor of Science degree in electrical engineering Summa Cum Laude from Brigham Young University, Provo, UT, in April 1993 and the Master of Science degree in electrical engineering, also from Brigham Young University, in August 1995. Since August 1995, he has been pursuing the Ph.D. degree in electrical engineering at the University of Illinois, Urbana.

Since August 1996, he has been employed by the Air Force Research Laboratory. His research interests are in the area of numerical techniques for electromagnetic problems.



Jian-Ming Jin (S'87–M'89–SM'94) received the B.S. and M.S. degrees in applied physics from Nanjing University, Nanjing, China, in 1982 and 1984, respectively, and the Ph.D. degree in electrical engineering from the University of Michigan, Ann Arbor, in 1989.

He is an Associate Professor of Electrical and Computer Engineering and Associate Director of the Center for Computational Electromagnetics at the University of Illinois at Urbana-Champaign (UIUC).

His name is listed in the UIUC's *List of Excellent Instructors*. He has published more than 70 articles in refereed journals and several book chapters, authored *The Finite Element Method in Electromagnetics* (New York: Wiley, 1993) and *Electromagnetic Analysis and Design in Magnetic Resonance Imaging* (Boca Raton, FL: CRC, 1998), and coauthored *Computation of Special Functions* (New York: Wiley, 1996). His current research interests include computational electromagnetics, scattering and antenna analysis, electromagnetic compatibility, and magnetic resonance imaging.

Dr. Jin is a member of Commission B of USNC/URSI, Tau Beta Pi, and International Society for Magnetic Resonance in Medicine. He is a recipient of a 1994 National Science Foundation Young Investigator Award and 1995 Office of Naval Research Young Investigator Award. He also received a 1997 Xerox Research Award from UIUC College of Engineering and was appointed as the first Henry Magnuski Outstanding Young Scholar in the Department of Electrical and Computer Engineering in 1998. He serves on the Editorial Board for *Electromagnetics Journal* and *Microwave and Optical Technology Letters*. He was the Symposium Cochairman and Technical Program Chairman of the 1997 and 1988 International Symposia on Applied Computational Electromagnetics, respectively. He served as an Associate Editor of the IEEE TRANSACTIONS ON ANTENNAS AND PROPAGATION from 1996 to 1998.